HiSST: 2nd International Conference on
High-Speed Vehicle Science & Technology
11–15 September 2022, Bruges, Belgium

Coupled fluid / thermal computation of ablating graphite material using nonequilibrium chemistry during atmospheric entry

Vivien Loridan[1], *Simon Peluchon*[2], *Jean Claudel*[3]

Abstract

The present work aims at improving the numerical prediction of graphite material degradation during an entire reentry phase. For this purpose, 2D axisymmetric simulations are carried out on the nosetip of the IRV-2 vehicle, which is a well-referred test case that employed a thermal protection system composed of non-charring carbon. The coupled fluid / thermal approach adopted for such aerothermodynamics computations is presented, as well as two different ablation models, which both rely on the heterogeneous reactions of oxidation and sublimation that occur on the heat shield of the vehicle. The first ablation paradigm is based on the B' tabulation, which has been historically used to assess the blowing rate of the recessing wall in the framework of a single gas (air) at chemical equilibrium. If such strategy has proven its reliability and efficiency over the past few decades, it suffers from many assumptions that are prone to be broken when applied to realistic descent trajectories. Such hypotheses include the consideration of a chemical equilibrium at the wall, a supposedly weak blowing rate, no injection of the ablated carbonaceous species into the flow, and the use of convective coefficients that directly depend on the boundary layer location. To overcome these aforementioned limitations, a more relevant ablation model, which takes care of the intrinsic multi-species nature of the flow, is proposed and implemented. The ablating mass flux and the species mass fractions at the wall, which are the product of finite-rate surface chemistry mechanisms, are accurately performed and updated at each convergence step of the flow. A particular emphasis is made on the generalization to chemical nonequilibrium, which leads to reducing the ablated surface thickness during a complete trajectory. In this perspective, the influence of the injected species that react with the surrounding flow is also investigated. Finally, the effects of different surface reaction schemes on the ablated surface shape and temperature are discussed.

Keywords: *aerothermodynamics, ablation, multi-species*

Nomenclature

Latin
c – Species mass fraction
$\widetilde{c}$ – Element mass fraction
$\dot{m}$ – Mass flow rate
E – Total energy
p – Pressure
t – Time
T – Temperature
τ_{xx}, τ_{xy}, τ_{yy} – Viscous stress components
u, v – Velocity components
x, y – Space coordinates
Greek
ϵ – Internal energy
κ – Conductivity
μ – Viscosity
ρ – Density
Subscripts
eq – Chemical equilibrium
e – Boundary layer edge
1 – First fluid cell upstream the wall
i – Species
k – Element
r – Reaction
c – Inviscid
v – Viscous
w – Wall property
F – Fluid property
S – Solid property

[1] *CEA-Cesta, 15 avenue des Sablières – CS 60001, 33116 Le Barp Cedex, vivien.loridan@cea.fr*
[2] *CEA-Cesta, 15 avenue des Sablières – CS 60001, 33116 Le Barp Cedex, simon.peluchon@cea.fr*
[3] *CEA-Cesta, 15 avenue des Sablières – CS 60001, 33116 Le Barp Cedex, jean.claudel@cea.fr*

1. Contextualization

During atmospheric entry, a spacecraft usually operates in hypersonic regime. Under such condition, a bow shock appears around the vehicle, inside which the flow is compressed and slowed down. The subsequent tremendous increase of temperature specifically initiates several physical processes such as ionization and dissociation of molecules. The high thermal flux imposed on the heat shield of the vehicle challenges the integrity of the payload. To prevent such potential damages, the thermal protection system (TPS) is typically designed to absorb an important part of the incoming energy via its gradual degradation during the entire reentry phase. To control such so-called ablation phenomenon, it is necessary to better understand the complex interactions between the flow and the solid occurring at the gas-solid interface. In this context, the present work aims at improving the numerical prediction of graphite material degradation during an entire reentry phase by using a strong coupling between computational fluid dynamics (CFD) and material thermal response (MTR). To take account of the variety of nonequilibrium effects at stake, the gas dynamics is presently characterized by a multi-species reacting flow.

Historically, simulations of ablation during reentry were performed with the use of material response codes loosely coupled to flow solvers, considering a gas at equilibrium. As far as we know, one of the first numerical approach used to predict ablation through gas-solid interaction was developed by the US Aerotherm Corporation in the late 60's. CFD was solved using a boundary layer approach (BLIMP code), which was loosely coupled with a MTR module (CMA code) that dealt with one-dimensional in-depth heat conduction. To quantify the physical processes at stake during the atmospheric entry of the IRV-2 vehicle, [1, 2] capitalized on the coupling between SACCARA, the finite-volume Navier-Stokes code from Sandia National Laboratory, and the 2D MTR code COYOTE II based on the Galerkin form of the finite element method. Their equilibrium surface chemistry ablation model relies on tables generated by the ACE code. More recently, [3] also take advantage of the aforementioned so-called B' tables (B standing for blowing) to revisit the graphite degradation of the nosetip of the IRV-2 spacecraft along its trajectory. They interfaced LEMANS, the CFD code developed at The University of Michigan, with MOPAR, the 1D MTR solver built on a control volume finite-element method. Other similar computations have been undertaken with the coupling of TITAN, a 2D MTR code [4], with GIANTS, a 2D Navier-Stokes solver incorporating thermochemistry surface boundary conditions [5]. The improvement of ablation models through the integration of a larger variety of physical processes is a current topic that has been devoted to a considerable effort from the scientific community. For example, [6, 7] incorporated an exhaustive chemistry model to take account of the effects of nonequilibrium chemistry within the gas in the framework of the Stardust vehicle reentry. They used the CFD code DPLR with the 1D MTR code FIAT, both developed at NASA Ames Research Center. It is nevertheless important to mention that thermochemical equilibrium at the wall was still assumed through the use of pre-computed ablation tables generated by the MAT code. [8, 9] investigated the improvements brought by fully coupled ablation-flowfield simulations compared with their loosely coupled counterparts. More particularly, [9] included a multi-elements gas model to account for equilibrium ablation during the reentry phase of the Orion Heatshield. Their works relied on LAURA, the flow solver developed at NASA Langley, which has been specifically extended with surface boundary conditions dedicated to ablation.

During these last few years, several developments have also emerged in CFD codes to tackle nonequilibrium surface chemistry. Among these interesting milestones, [10, 11] performed simulations of hypersonic reacting flows including thermochemical nonequilibrium effects at only a few selected points taken respectively form the trajectory of the Stardust and the IRV-2 reentry vehicles. They took advantage of the strongly coupled LEMANS and MOPAR codes to reproduce the complex interactions between the flow and the heatshield.

In the context of these previous studies, the present work aims at improving the numerical prediction of graphite material degradation during an entire reentry phase with the use of a strongly-coupled ablating flow paradigm including nonequilibrium effects. We first emphasize the inherent limitations related to the loosely-coupled ablation models. If such procedures turned out to be computationally efficient, they intrinsically rely on a thin-film transfer theory and are thus dependent on semi-empirical recovery

parameters that cannot be extended to entire realistic descent trajectories. They also do not include the blowing of carbonaceous species from material degradation into the surrounding flow. For these reasons, a more exhaustive ablation model has been developed, which is fully coupled with the nonequilibrium multi-species reacting flow.

The present work is organized as follows. On the first hand, the historical ablation strategy based on the B' tables, as well as the multi-species formulation at stake in the present work, are described. On the other hand, 2D axisymmetric simulations related to the trajectory of the IRV-2 vehicle [2, 8, 11] are presented to validate the multi-species ablation approach, confirming its reliability to predict the complex gas-solid interactions at stakes during atmospheric entry.

2. Aerothermal coupling

The aerothermal code used in this study includes a Navier-Stokes solver (CFD) and a heat conduction module for the material (MTR) that are strongly coupled and embedded in the same numerical platform.

2.1. Navier-Stokes solver

The CFD solver currently developed at CEA-CESTA solves 2D-axisymmetric and 3D Navier-Stokes equations for flows in chemical equilibrium (the surrounding air being treated as a single species) or nonequilibrium (multi-species reacting flows). Thermal equilibrium (single temperature) is nevertheless assumed.

The conservation equations at stake can commonly be written under the following conservative form

$$\frac{\partial \boldsymbol{U}}{\partial t} + \boldsymbol{\nabla} \cdot \underline{\underline{F}} = \boldsymbol{S}. \tag{1}$$

The vector of conserved variables $\boldsymbol{U}$ and the vector of source terms $\boldsymbol{S}$ are respectively

$$\boldsymbol{U} = \begin{pmatrix} \rho_i \\ \rho \boldsymbol{v} \\ \rho E \end{pmatrix}, \text{ and } S = \begin{pmatrix} \dot{\omega}_i \\ \boldsymbol{0} \\ 0 \end{pmatrix},$$

for which ρ_i is the density of species i (with $i = 1, ..., n_s$), ρ is the total gas density, $\boldsymbol{v}$ is the bulk velocity field, E is the total energy given by

$$E = \epsilon + \frac{1}{2} (\boldsymbol{v} \cdot \boldsymbol{v})$$

where ϵ is the internal energy of the gas. The source term $\dot{\omega}_i$, which governs the gain or loss of species i through chemical reactions, is written as

$$\dot{\omega}_i = M_i \sum_{r=1}^{n_r} \left(\nu_{ir}^{''} - \nu_{ir}^{'} \right) \left(k_r^f \prod_{s=1}^{n_s} \left(\frac{\rho_s}{M_s} \right)^{\nu_{sr}^{'}} - k_r^b \prod_{s=1}^{n_s} \left(\frac{\rho_s}{M_s} \right)^{\nu_{sr}^{''}} \right)$$

with M_s being the molar mass of species s and where $\nu_{sr}^{'}$ and $\nu_{sr}^{''}$ are respectively the forward and backward stoechiometric coefficients involved in reaction r, written in general form as

$$\sum_{s=1}^{n_s} \nu_{sr}^{'} R_s \rightleftharpoons \sum_{s=1}^{n_s} \nu_{sr}^{''} R_s$$

for $r = 1, ..., n_r$, with n_r the total number of reactions and R_s being either the reactants (left-hand side) or products (right-hand side) related to reaction r. The forward reaction rate k_r^f for reaction r is expressed by the Arrhenius law

$$k_r^f = A_r^f T^{B_r^f} \exp\left(-\frac{T_{ar}^f}{T} \right), \tag{2}$$

for which T is the gas temperature and T_{ar} is the activation temperature for reaction r. Coefficients A_r^f and B_r^f are also related to reaction r and are typically tabulated. The backward reaction rate k_r^b for reaction r is deduced from k_r^f via the relation $k_r^b = k_r^f / K_r$, for which K_r is the equilibrium constant of reaction r commonly defined in terms of species densities as

$$K_r = \frac{\prod_{s=1}^{n_s} \left(\frac{\rho_k}{M_k}\right)_{\text{eq}}^{\nu_{sr}''}}{\prod_{s=1}^{n_s} \left(\frac{\rho_k}{M_k}\right)_{\text{eq}}^{\nu_{sr}'}}$$

where subscript eq is related to quantities evaluated at chemical equilibrium. In practice, K_r is tabulated with temperature according to

$$K_r = \left(\frac{p^0}{RT}\right)^{\sum_{s(r)} \Delta\nu_s} \exp\left(-\frac{\sum_{s(r)} \Delta\nu_s \Delta G_s^0(T)}{RT}\right) = \left(\frac{P^0}{RT}\right)^{\sum_{s(r)} \Delta\nu_s} 10^{\sum_{s(r)} \Delta\nu_s K_s^{\text{JANAF}}}$$

with p^0 the atmospheric pressure, ΔG_s^0 the Gibbs free energy, $\Delta\nu_s = \nu_{sr}'' - \nu_{sr}'$ and

$$K_s^{\text{JANAF}} = \frac{1}{\ln(10)} \left(-\frac{\Delta G_s^0(T)}{RT}\right),$$

the equilibrium coefficient of species s taken from the JANAF tables [12].

The flux tensor in the Navier-Stokes equation (1) is $\underline{\underline{F}} = \underline{\underline{F}}_c - \underline{\underline{F}}_v$, which is written as the contribution of the inviscid flux $\underline{\underline{F}}_c$ and the viscous flux $\underline{\underline{F}}_v$ respectively given by

$$\underline{\underline{F}}_c = \begin{pmatrix} \rho_i \boldsymbol{v} \\ \rho \boldsymbol{v} \otimes \boldsymbol{v} + p \underline{\underline{I}} \\ \rho H \boldsymbol{v} \end{pmatrix} \text{ and } \underline{\underline{F}}_v = \begin{pmatrix} -\boldsymbol{J}_i \\ \underline{\underline{\tau}} \\ -\boldsymbol{q} + \underline{\underline{\tau}} \boldsymbol{v} \end{pmatrix},$$

with p being the pressure, $\underline{\underline{\tau}}$ the shear stress tensor and $H = E + p/\rho$ the total enthalpy. Mass fluxes are modeled according to Fick's law

$$\boldsymbol{J}_i = -\rho D_i \boldsymbol{\nabla} c_i,$$

for which c_i is the mass fraction of species i. The viscous stress tensor is related to a Newtonian fluid via

$$\underline{\underline{\tau}} = \mu \left[(\boldsymbol{\nabla} \otimes \boldsymbol{v}) + (\boldsymbol{\nabla} \otimes \boldsymbol{v})^\top \right] + \lambda \left(\boldsymbol{\nabla} \cdot \boldsymbol{v} \right) \underline{\underline{I}}.$$

Heat fluxes involved in the energy conservation equation are modeled according to Fourier's law

$$\boldsymbol{q} = -\kappa \boldsymbol{\nabla} T + \sum_i \boldsymbol{J}_i h_i,$$

including the contribution of thermal conduction and diffusion.

In the above formulations, $\lambda = -2/3\,\mu$ according to Stokes' hypothesis. The mixture viscosity μ is obtained via Wilke's semi-empirical mixing rule [13] with species viscosities calculated using Blottner's model [14]. The mixture conductivity κ is obtained using Prandtl's relation $\kappa = \mu C_p / P_r$ with Prandtl number $P_r = 0.67$ and the diffusivity model for each species is given by the Lewis model $\rho D = \kappa L_e / C_p$ for which C_p is the specific heat at constant pressure. In what follows, the Lewis number is set to $L_e = 1.4$.

From the calculated conserved variables, the physical quantities ρ, c_i, u, v, T and p are deduced. The total gas density is simply given by $\rho = \sum_i \rho_i$, allowing to determine the velocity components u and

v, as well as the species mass fractions c_i that are calculated as $c_i = \rho_i/\rho$. The gas temperature T is calculated with the knowledge of the internal energy ϵ via an iterative Newton method by equating $E - 1/2\ (\boldsymbol{v} \cdot \boldsymbol{v}) = \epsilon(T)$. In the present study, the internal energy is evaluated via

$$\epsilon = \sum_i c_i \epsilon_i(T),$$

for which the species internal energy ϵ_i is tabulated with temperature via the use of the Glenn coefficients [15], including the contribution of the translational, rotational, vibrational and electronic excitation energy modes. The pressure p is calculated assuming that each species can be modeled using a perfect gas relation and Dalton's law of partial pressures so that $p = \sum_i p_i = \sum_i \rho_i RT/M_i$.

Let us mention that for the case of a gas at equilibrium, only one pseudo-species ($i = 1$ for air) is considered. Therefore, the previous Navier-Stokes description is reduced with $c_i = 1$, $\dot{\omega}_i = 0$, $\boldsymbol{J}_i = \boldsymbol{0}$, and $\boldsymbol{q} = -\kappa\, \boldsymbol{\nabla} T$.

Numerically, the code employs multi-block structured grids. A finite-volume formulation is used for the inviscid fluxes, which are typically discretized according to a modified version of the Roe scheme that turned out to be particularly adapted for shock capturing (carbuncle-free) and the treatment of multi-species reacting flows. The viscous fluxes are described with a finite-difference paradigm that employs a standard, second-order, central differencing scheme. The solution of the Navier-Stokes equations is driven to its steady state through a implicit resolution, which requires to calculate the Jacobian matrices related to the inviscid and viscous flux tensors and the source term. Such implicit solver allows agressive CFL ramping and proved its efficiency in the context of High Performance Computing (HPC).

2.2. Material thermal response module

The material thermal response module solves 2D-axisymmetric and 3D heat conduction in the solid, written under the conservative form as

$$\frac{\partial}{\partial t}\left(\rho E\right)_s + \boldsymbol{\nabla} \cdot \boldsymbol{F}_s = 0,$$

for which E_s is the energy related to the material. The flux vector $\boldsymbol{F}_s$ is written in terms of the heat flux $\boldsymbol{q}_s$ as $\boldsymbol{F}_s = -\boldsymbol{q}_s$, with $\boldsymbol{q}_s$ being modeled according to Fourier's law

$$\boldsymbol{q}_s = -\kappa_s \boldsymbol{\nabla} T_s.$$

The temperature T_s inside the solid is deduced from E_s via

$$E_s = \int_{T_0}^{T_s} C_{ps}\, \mathrm{d}T',$$

for which C_{ps} are known quantities that are tabulated with temperature T_s accordingly to the TPS material at stake.

Similarly to the flow solver, the energy diffusion equation is solved on a multi-block structured grid. The heat fluxes are discretized via a second-order central differencing scheme. The numerical resolution inside the TPS remains implicit, but contrary to the flow resolution, thermal diffusion is unsteady.

2.3. Coupling implementation

Simulations that are carried out to predict the material ablation of the heat shield of a vehicle during a reentry phase rely on a coupled fluid / thermal approach. From the characteristic timescales related to convection, conduction, diffusion and blowing inside the gas boundary layer, as well as the conducting and ablating effects inside the material, the flow dynamics is, as mentioned earlier, considered steady whereas the heat transport in the TPS is considered unsteady. The coupling rate between the flow and the material is thus primarily governed by the timescales related to surface recession (ablation).

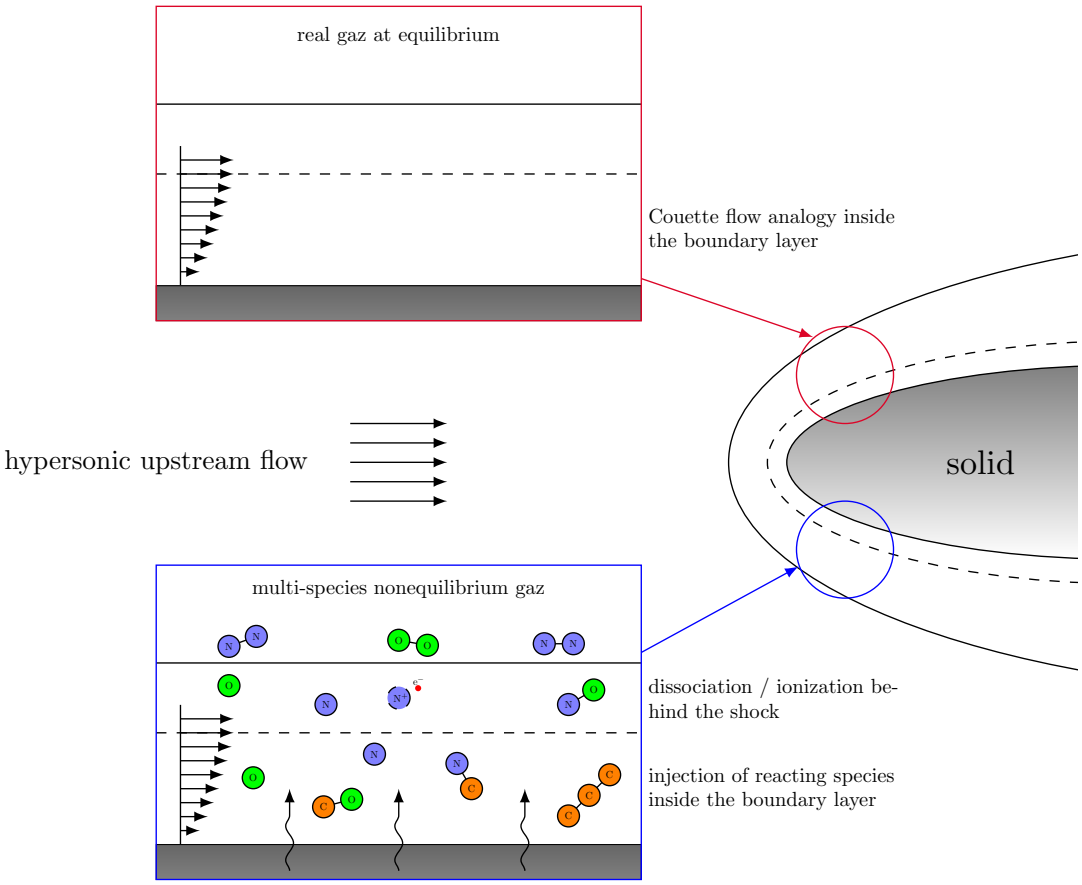

Fig 1. Different strategies at stakes used in the flow solver to model ablation. (top) the flow is supposed to be at equilibrium and is represented by a single real gas (air). A Couette flow analogy is required to compensate for the model deficiencies to grasp the ablation phenomenon. (bottom) nonequilibrium flow represented by a multi-species reacting gas. In this case, no assumptions are needed since injections and blowing at the gas-solid interface is strongly coupled with the flow dynamics, enabling to fully determine the ablation rates.

Two options can be used according to how the gas is modeled by the flow solver. First, the gas is considered at chemical equilibrium and is described by a single pseudo-species. In this case, the blowing effect is only considered in the ablation model to derive a recession rate and to adjust the wall heat flux as a boundary condition for the solid resolution. The injection of carbonaceous species from the solid to the gas boundary layer, however, is entirely discarded through the flow resolution, as illustrated in Fig. 1. As pointed out in the next section, additional assumptions derived from a Couette flow analogy are necessary to recover the shortcomings of the model.

In the second option, the gas is treated as a multi-species reacting flow. The carbonaceous species expelled from the wall by graphite degradation are therefore completely integrated in the flow resolution, as emphasized by Fig. 1. They can react with the air species via endothermic or exothermic chemical reactions, thus influencing the flow dynamics inside the boundary layer, which in turn impacts the heat transfer at the gas-solid interface and eventually thermal conduction into the material. With this last strategy, the coupling flow / material is enforced compared with the previous equilibrium situation.

The physical quantities exchanged at the interface between the fluid and the thermal protection system (TPS) are derived from mass and energy balances at the surface at each time step.

The coupling procedure for a multi-species reacting flow is performed as follows. First, the surface mass balance (SMB) equation is solved, enabling to deduce the ablation mass flow rate, as well as the mass fraction of the species at the wall expelled into the flow from the degradation of the heat shield. The latter are considered as boundary conditions for the Navier-Stokes system of equations, which is treated by the CFD module towards its steady state. The surface energy balance (SEB) equation is then considered to relate the heat flux conducted from the surface into the solid with the convective wall heat flux that has been calculated during the aforementioned hydrodynamic step. Such thermal conductive flux serves as a boundary condition for the time-dependent material response module that specifically computes the heat conduction into the vehicle. Once the heat transfer equation is solved inside the TPS, a new surface temperature is deduced, which is used as a wall boundary condition for the next time-step of the coupled fluid / solid iterative process. The total mass flow rate $\dot{m}$ obtained after each computational loop enables to calculate the wall recession rate v_w via the relation $v_w = \dot{m}/\rho_s$ (ρ_s being the density of the solid). The corresponding mesh displacement is therefore derived to adjust the shape of the vehicle in accordance with the ablation rate.

With such algorithm, the thermal response code is directly integrated as a boundary condition of the Navier-Stokes solver, thus taking advantage of the implicit nature of the code as well as the aggressive CFL ramping.

2.4. Derivation of the general wall boundary conditions

To ensure the coupling procedure described above, relevant surface boundary conditions have to be considered. Their derivation follows the method detailed in [16], for which balance equations used to put forward boundary conditions between two adjoining domains of different natures are established via flux balancing at the interface. In order to unify the mathematical formulation for both the flow and the solid, we choose to describe both domains by the general Navier-Stokes equations (1) written under the integral form as

$$\iiint_{\Omega} \frac{\partial \boldsymbol{U}}{\partial t} \mathrm{d}\mathcal{V} + \oiint_{\delta\Omega} \underline{\underline{F}}\, \boldsymbol{n}\, \mathrm{d}\mathcal{S} = \iiint_{\Omega} \boldsymbol{S}\, \mathrm{d}V,$$

for which Ω is the volume of the cell, $\delta\Omega$ is the surface of the cell and $\boldsymbol{n}$ is the outward-pointing surface normal vector.

Let us first consider a 2D cell of dimensions $(\delta x \times \delta y)$ that interfaces the fluid and solid, as illustrated in Fig. 2. With such cartesian mesh, the normal surface vectors for each boundary are respectively given by $n_1 = (0, 1)$ and $n_3 = (0, -1)$ for the two boundaries along the wall and respectively by $n_2 = (1, 0)$ and $n_4 = (-1, 0)$ for the two boundaries transverse to the wall.

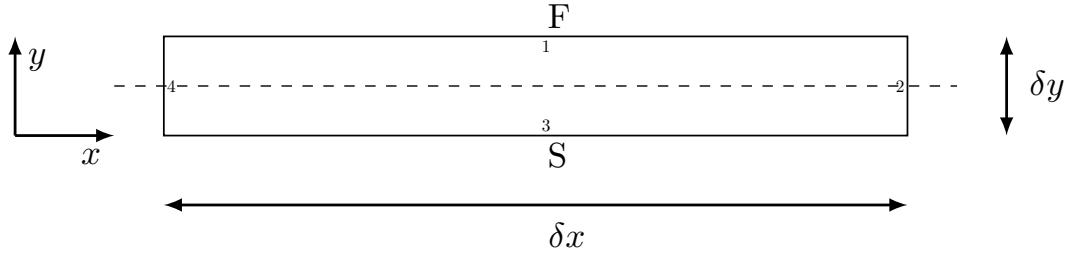

Fig 2. Interface cell between the fluid domain and solid domain, with the dashed line representing the gas-surface boundary (wall).

Taking account of the directions related to the aforementioned normal surface vectors, the projection of

the general Navier-Stokes system onto the interface cell of Fig. 2 gives

$$
\begin{aligned}
&\int_{-\delta x/2}^{+\delta x/2}\int_{-\delta y/2}^{+\delta y/2}\frac{\partial}{\partial t}\begin{pmatrix}\rho c_i\\ \rho u\\ \rho v\\ \rho E\end{pmatrix}\mathrm{d}x\mathrm{d}y\\
&=-\int_{-\delta x/2}^{+\delta x/2}\begin{pmatrix}\rho c_i u + J_{xi} & \rho c_i v + J_{yi}\\ \rho u^2+p-\tau_{xx} & \rho uv-\tau_{xy}\\ \rho uv-\tau_{xy} & \rho v^2+p-\tau_{yy}\\ \rho H u-\tau_{xx}u-\tau_{xy}v+q_x & \rho H v-\tau_{xy}u-\tau_{yy}v+q_y\end{pmatrix}_{y=+\delta y/2}\begin{pmatrix}0\\ +1\end{pmatrix}\mathrm{d}x\\
&\quad-\int_{-\delta y/2}^{+\delta y/2}\begin{pmatrix}\rho c_i u + J_{xi} & \rho c_i v + J_{yi}\\ \rho u^2+p-\tau_{xx} & \rho uv-\tau_{xy}\\ \rho uv-\tau_{xy} & \rho v^2+p-\tau_{yy}\\ \rho H u-\tau_{xx}u-\tau_{xy}v+q_x & \rho H v-\tau_{xy}u-\tau_{yy}v+q_y\end{pmatrix}_{x=+\delta x/2}\begin{pmatrix}+1\\ 0\end{pmatrix}\mathrm{d}y\\
&\quad-\int_{-\delta x/2}^{+\delta x/2}\begin{pmatrix}\rho c_i u + J_{xi} & \rho c_i v + J_{yi}\\ \rho u^2+p-\tau_{xx} & \rho uv-\tau_{xy}\\ \rho uv-\tau_{xy} & \rho v^2+p-\tau_{yy}\\ \rho H u-\tau_{xx}u-\tau_{xy}v+q_x & \rho H v-\tau_{xy}u-\tau_{yy}v+q_y\end{pmatrix}_{y=-\delta y/2}\begin{pmatrix}0\\ -1\end{pmatrix}\mathrm{d}x\\
&\quad-\int_{-\delta y/2}^{+\delta y/2}\begin{pmatrix}\rho c_i u + J_{xi} & \rho c_i v + J_{yi}\\ \rho u^2+p-\tau_{xx} & \rho uv-\tau_{xy}\\ \rho uv-\tau_{xy} & \rho v^2+p-\tau_{yy}\\ \rho H u-\tau_{xx}u-\tau_{xy}v+q_x & \rho H v-\tau_{xy}u-\tau_{yy}v+q_y\end{pmatrix}_{x=-\delta x/2}\begin{pmatrix}-1\\ 0\end{pmatrix}\mathrm{d}y\\
&\quad+\int_{-\delta x/2}^{+\delta x/2}\int_{-\delta y/2}^{+\delta y/2}\begin{pmatrix}\dot{\omega}_i\\ 0\\ 0\\ 0\end{pmatrix}\mathrm{d}x\mathrm{d}y,
\end{aligned}
$$

for which the cell boundary located at $y=-\delta y/2$ is inside the solid and the one located at $y=+\delta y/2$ lays within the flow. Such system eventually leads to the following wall boundary conditions

$$
\begin{cases}
\delta y\,\dfrac{\partial \rho}{\partial t} &= -\left[\rho v\right]_F+\left[\rho v\right]_S=0\\
\delta y\,\dfrac{\partial}{\partial t}(\rho c_i) &= -\left[\rho c_i v+J_{yi}\right]_F+\left[\rho c_i v+J_{yi}\right]_S+\delta y\,\dot{\omega}_i\\
\delta y\,\dfrac{\partial}{\partial t}(\rho u) &= -\left[\rho uv-\tau_{xy}\right]_F+\left[\rho uv-\tau_{xy}\right]_S\\
\delta y\,\dfrac{\partial}{\partial t}(\rho v) &= -\left[\rho v^2+p-\tau_{yy}\right]_F+\left[\rho v^2+p-\tau_{yy}\right]_S\\
\delta y\,\dfrac{\partial}{\partial t}(\rho E) &= -\left[\rho H v-\tau_{xy}u-\tau_{yy}v+q_y\right]_F+\left[\rho H v-\tau_{xy}u-\tau_{yy}v+q_y\right]_S,
\end{cases}
$$

for which subscript F relates to the fluid domain and subscript S relates to the solid domain. Knowing that the mass flow rate is given by $\dot{m}=[\rho v]_F=[\rho v]_S$, and taking account of $[J_{yi}]_S=0$, $[\tau_{xx}]_S=0$, $[\tau_{xy}]_S=0$, $[\tau_{yy}]_S=0$ and $[\dot{m}c_i]_S=\dot{m}_i$, the conservation equations projected on the cells around the

wall give

$$\begin{cases} \delta y \dfrac{\partial}{\partial t}(\rho c_i) &= -\left[\dot{m} c_i + J_{yi}\right]_F + \dot{m}_i + \delta y \, \dot{\omega}_i \\ \delta y \dfrac{\partial}{\partial t}(\rho u) &= -\left[\dot{m} u - \tau_{xy}\right]_F + \left[\dot{m} u\right]_S \\ \delta y \dfrac{\partial}{\partial t}(\rho v) &= -\left[\dot{m} v + p - \tau_{yy}\right]_F + \left[\dot{m} v + p\right]_S \\ \delta y \dfrac{\partial}{\partial t}(\rho E) &= -\left[\dot{m} H - \tau_{xy} u - \tau_{yy} v + q_y\right]_F + \left[\dot{m} H + q_y\right]_S . \end{cases} \tag{3}$$

Let us mention that the radiative fluxes have deliberately been neglected in the present study.

Written in this formalism, such surface boundary conditions are well adapted for a multi-species description of the flow, as emphasized in the next section. For a flow described by a single gas at equilibrium for example (onto which the historical ablation model relies), the presented wall boundary conditions are over-detailed and involve quantities that cannot be used as such by the equilibrium gas module. The wall mass flux J_{yi} and the wall heat flux q_y are indeed not directly known since no blowing or injection of carbonaceous species are taken into account by the flow solver. To tackle these deficiencies, the historical ablation model needs to invoke blowing assumptions to relate the unknown blown parameters (such as wall mass and heat fluxes) with the unblown fluxes the solver is able to calculate, as described below.

3. Historical and multi-species ablation models

3.1. Historical ablation model

The historical ablation model is based on B' tables, which contain all the necessary assumptions the algorithm needs to correctly compute ablation via a loosely coupled approach.

3.1.1. Couette flow without blowing

The theoretical framework of the historical ablation model relies on a formalism inspired by a Couette flow. It simply consists of a incompressible fluid flowing between two parallel planar plates separated by a length δle, the upper plate moving with a speed u_e, as depicted in Fig. 3. Such situation roughly reproduces the behavior of a flow inside the boundary layer, for which δle represents the width of the boundary layer, the lower plate represents the wall of the vehicle and the upper plate represents the immediate upstream of the boundary layer. The boundary conditions give mass fractions c_{iw0} and temperature T_w at the wall, as well as mass fractions c_{ie} and temperature T_e at the upper plate (corresponding to the boundary layer edge).

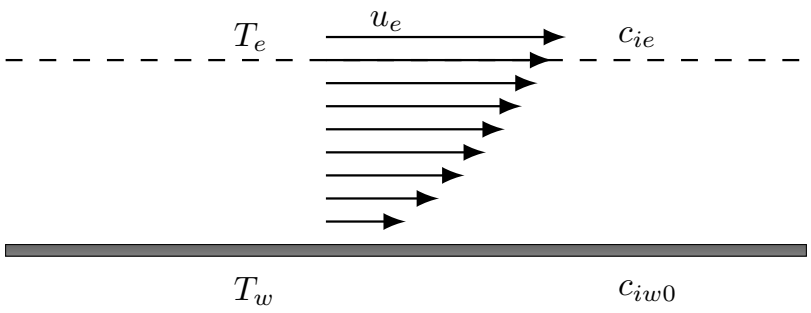

Fig 3. Couette flow without blowing. The lower plate can be assimilated to the vehicle wall and the upper plate represents the edge of the boundary layer.

If both the Prandl and Lewis number are supposed to be equal to unity, a strong analogy can be analytically established between mass and heat transfer, as shown below. The mass species conservation equation writes

$$-\frac{\partial}{\partial y}\left(\rho D\,\frac{\partial c_i}{\partial y}\right)=0,$$

which leads to the wall mass flux J_{i0} expressed by

$$J_{i0}=-\,\rho D\,\frac{\partial c_i}{\partial y}\bigg|_w=-\alpha_0\,\left(c_{ie}-c_{iw0}\right),$$

with $\alpha_0=\rho D/\delta l_e$. Similarly, the energy conservation equation writes (keeping in mind that $P_r=L_e=1$)

$$-\frac{\partial}{\partial y}\left(\mu\,\frac{\partial H}{\partial y}\right)=0$$

with the wall heat flux given by

$$q_0=-\,\lambda\,\frac{\partial T}{\partial y}\bigg|_w-\sum_i \rho D h_i\,\frac{\partial c_i}{\partial y}\bigg|_w=-\alpha_0\,\left(H_e-H_{w0}\right). \tag{4}$$

Both mass and heat flux, which are easily expressed in terms of the imposed boundary conditions, involve the α_0 parameter. The latter is commonly referred as the unblown convective coefficient.

3.1.2. Couette flow with blowing

If a blowing rate is now applied transversely to the wall via a new flow velocity component v, as described in Fig. 4, a strong analogy between mass and heat transfer still remains.

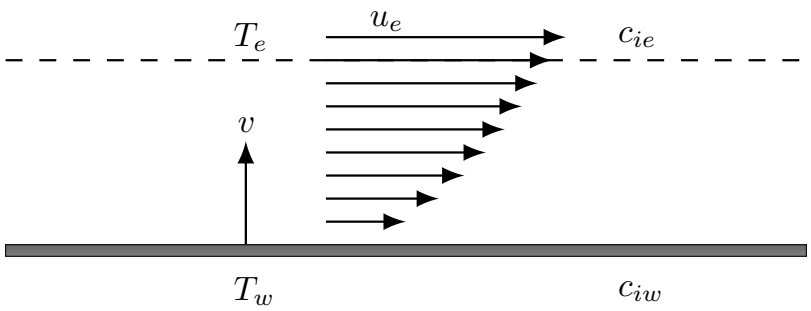

Fig 4. Couette flow with blowing. The lower plate can be assimilated to the vehicle wall and the upper plate represents the edge of the boundary layer. Blowing is characterized by a supplementary velocity component v transverse to the wall.

In this case, the mass species conservation equation writes

$$\frac{\partial}{\partial y}\left(\rho c_i v\right)-\frac{\partial}{\partial y}\left(\rho D\,\frac{\partial c_i}{\partial y}\right)=0,$$

which leads to the corresponding wall mass flux J_i expressed by

$$J_i=-\,\rho D\,\frac{\partial c_i}{\partial y}\bigg|_w=-\alpha\,\left(c_{ie}-c_{iw}\right), \tag{5}$$

for which c_{iw} is the species mass fractions at the wall when blowing occurs. In the above expression, the blown convective coefficient α is expressed as

$$\alpha = \frac{\dot{m}}{\exp(\dot{m}/\alpha_0) - 1} \tag{6}$$

with $\dot{m} = \rho v$. The energy conservation equation writes (under the hypothesis of $P_r = L_e = 1$)

$$\frac{\partial}{\partial y}\left(\rho v H\right) - \frac{\partial}{\partial y}\left(\mu \frac{\partial H}{\partial y}\right) = 0$$

with the wall heat flux given by

$$q = -\lambda \left.\frac{\partial T}{\partial y}\right|_w - \sum_i \rho D h_i \left.\frac{\partial c_i}{\partial y}\right|_w = -\alpha \left(H_e - H_w\right).$$

Under such framework, the blown fluxes can easily be related to their unblown counterparts [17] according to

$$J_i = \left(\alpha/\alpha_0\right) J_{i0} - \alpha \left(c_{iw0} - c_{iw}\right)$$

and

$$q = \left(\alpha/\alpha_0\right) q_0 - \alpha \left(H_{w0} - H_w\right).$$

3.1.3. Generalization

The historical ablation model currently implemented in the fluid / thermal algorithm generalizes Eq. (4) by defining the unblown convective coefficient α_0 via the calculated unblown wall heat flux q_0 through

$$\alpha_0 = -\frac{q_0}{H_a - H_{w0}},$$

with H_a the adiabatic wall enthalpy [18], which is defined as a correction to the enthalphy of the boundary layer H_e through a recovery factor r taken from experimental correlations, such that $H_a = h_a + u_e^2/2$ with $h_a = h_e + (r-1)u_e^2/2$ [17]. From such definition, numerical instabilities can clearly be encountered if H_a is close to H_{w0}. The blown convective coefficient α is also extended from Eq. (6) via the relation

$$\alpha = \frac{2\eta\dot{m}}{\exp\left(2\eta\dot{m}/\alpha_0\right) - 1} \sim \alpha_0 - \eta\,\dot{m},$$

for which η is an adjustment parameter based on experimental correlations that have been operated at the stagnation point of a sphere geometry [17]. The linearization made in the right-hand side of the above expression also assumes that the injection is weak ($\dot{m} \ll \alpha_0$), which can be a questionable hypothesis. Besides the aforementioned possible numerical instabilities, the historical model is based on phenomenological parameters (η, H_a) that are mostly restricted to sphere-cone geometries and thus may not be extended and applied as such to realistic atmospheric entry related simulations. All these limitations have driven the need to build a more robust and relevant ablation model.

3.1.4. Mass conservation

By using the expression of the wall mass flux written via the boundary layer quantities (5), the surface mass balance equation in Eq. (3) gives for the historical ablation model

$$\frac{\partial c_i}{\partial t} = -\left(\frac{\dot{m} + \alpha}{\rho \delta y}\right) c_i + \left(\frac{\dot{m}_i + \alpha\, c_{ie}}{\rho \delta y}\right) + \frac{\dot{\omega}_i}{\rho} \tag{7}$$

with $\dot{m} = \sum_i \dot{m}_i$.

Because of the different timescales at stake, the mass balance equation is a stiff system of first-order Ordinary Differential Equations (ODE), which is solved using an implicit Runge-Kutta method of order 5 at long time (i.e. until convergence is reached).

If equilibrium is assumed at the wall, it can be more advantageous to solve the mass conservation equation in terms of element mass fractions $\widetilde{c}_k$ instead of species mass fractions c_i. In this case, the governing ODE is

$$\frac{\partial \widetilde{c}_k}{\partial t} = -\left(\frac{\dot{m}+\alpha}{\rho\delta y}\right)\widetilde{c}_k + \left(\frac{\dot{\widetilde{m}}_k + \alpha\,\widetilde{c}_{ke}}{\rho\delta y}\right), \tag{8}$$

with $\widetilde{c}_k = \sum_{i=1}^{n_e} a_i^k \left(\widetilde{M}_k/M_i\right) c_i$ and $\dot{\widetilde{m}}_k = \sum_{i=1}^{n_s} a_i^k \left(\widetilde{M}_k/M_i\right) \dot{m}_i$, for which the a_i^k coefficient is the number of element k in species i. Such equilibrium hypothesis is only valid if the timescale related to chemistry is much shorter than the timescales related to diffusion ($\rho\delta y/\alpha$) and ablation ($\rho\delta y/\dot{m}$). Once the element mass fractions have been calculated, the species mass fractions are deduced via the use of the *Mutation++* library [19].

3.1.5. Momentum conservation

Since the wall recession rate v_w is less smaller than the blown flow velocity v at the wall, the momentum conservation equation in Eq. (3) reduces, at steady state, to $p_S = p + \dot{m}v - \tau_{yy}$, which in practice is equivalent to

$$p_S = p_F.$$

3.1.6. Energy conservation

At steady state, the energy conservation equation in Eq. (3) writes

$$\left[\dot{m}H - \tau_{xy}u - \tau_{yy}v + q_y\right]_F = \left[\dot{m}H + q_y\right]_S.$$

Neglecting the shear stress components, and taking the corresponding relation between the blown and unblown wall heat fluxes for the historical ablation model, the energy balance equation gives

$$\left[q_y\right]_S = (\alpha/\alpha_0)\,\left[q_{0y}\right]_F - \dot{m}\Delta H_a,$$

for which the apparent enthalpy flux $\dot{m}\Delta H_a$ is given by $\dot{m}\Delta H_a = \alpha\,(H_{F0} - H_F) + \dot{m}\,(H_S - H_F)$ [17], with $H_{F0} = \sum_i c_{i0}h_i$, $H_F = \sum_i c_i h_i$ and H_S being respectively the enthalpy of fluid (without and with blowing) and solid.

The successive resolutions of the mass balance equation for different given pressures, temperatures and unblown convective coefficients α_0 enable to find the corresponding c_i at the wall, from which the $\dot{m}_i$ and the total mass flow rate $\dot{m} = \sum_i \dot{m}_i$ are deduced. The blown convective coefficient $\alpha = \alpha_0 - \eta\dot{m}$ is then found, as well as $\dot{m}\Delta H_a$ given above. With all of these ingredients, the so-called B' ablation tables that group the calculated physical quantities $(c_i, \dot{m}, \alpha, \dot{m}\Delta H_a)$ in terms of the parameters (P, T_w, α_0) are generated to feed the historical ablation model.

3.2. Multi-species ablation model

As a need for a more robust model to remove the dependencies of phenomenological parameters (η, H_a) and avoid numerical instabilities that can be encountered if $H_a = H_{w0}$, the so-called multi-species ablation model has been developed. It relies on the general surface balance equations described below.

3.2.1. Mass conservation

If the wall mass flux is now considered more generally as

$$\left[J_{yi}\right]_F = -\rho D\,\frac{c_{i1} - c_i}{\delta l_1}$$

relating quantities at the wall, c_i, and at the first fluid cell, c_{i1} (δl_1 is the width of the first fluid cell after the wall), the species mass conservation gives

$$\frac{\partial c_i}{\partial t} = -\left(\frac{\dot{m} + \dfrac{\rho D}{\delta l_1}}{\rho \delta y}\right) c_i + \left(\frac{\dot{m}_i + \dfrac{\rho D}{\delta l_1} c_{i1}}{\rho \delta y}\right) + \frac{\dot{\omega}_i}{\rho}, \tag{9}$$

where δy is the width of the control volume, D is the diffusion coefficient (calculated using a Lewis formulation) and $\dot{\omega}_i$ is the chemical source term related to the homogeneous reactions. Again, if chemical equilibrium is assumed at the wall, the mass conservation equation is preferentially written in terms of element mass fraction as

$$\frac{\partial \widetilde{c}_k}{\partial t} = -\left(\frac{\dot{m} + \dfrac{\rho D}{\delta l_1}}{\rho \delta y}\right) \widetilde{c}_k + \left(\frac{\dot{\widetilde{m}}_k + \dfrac{\rho D}{\delta l_1} \widetilde{c}_{k1}}{\rho \delta y}\right). \tag{10}$$

The mass balance equation is now fully integrated to the flow module and is solved at each hydrodynamic convergence step using an implicit Runge-Kutta method of order 5.

3.2.2. Energy conservation

The simplified surface energy balance equation (steady state ablation) used to relate the conductive heat flux $[q_y]_S$ with the wall convective flux $[q_y]_F$ is written as

$$[q_y]_S = [q_y]_F - \dot{m}\,(H_S - H_F)\,.$$

Exhibiting the energy balance equation into this specific formulation simply illustrates that the energy absorbed by the removal of material from the surface is not used to heat the TPS, thus keeping the vehicle wall at a relatively moderate temperature.

4. Validation of the multi-species ablation model

4.1. Presentation of the IRV-2 test case

In order to attest the reliability of the multi-species ablation model, 2D axisymmetric simulations are carried out on the IRV-2 vehicle, which is a well-referred test case that employed a TPS composed of non-charring carbon [1, 2, 8, 11]. The IRV-2 vehicle is a sphere-biconic with a nose radius of 0.01905 m and total length of 1.386 m, as shown in Fig. 5. The biconic angles are 8.42 and 6.10 deg, respectively, with the break occurring at an axial location of 0.1488 m measured from the stagnation point. For the purpose of corroborating our simulations with previously published results, the freestream conditions considered in the present work are taken from [2], which are illustrated in Fig. 5. Let us point out that such considered trajectory is not exactly the one followed by the IRV-2 vehicle during its actual flight, as the freestream conditions have been artificially re-adjusted in [2] to ensure the stability of their computations.

The present work only focuses on the IRV-2 nosetip (sphere and first cone). The mesh used to obtain axisymmetric solutions of the flow around the forebody of the vehicle contains 250 cells in the axial direction and 88 cells along the body, on a grid moving with the recessing surface. The flow on the nosetip is assumed to be completely laminar during the trajectory. The presented computations are obtained either with the historical ablation model and with the more exhaustive multi-species ablation model.

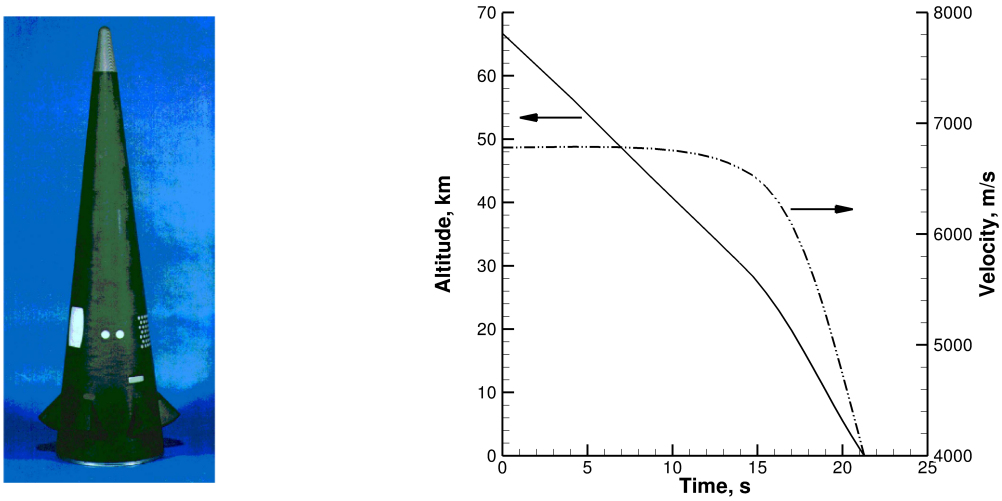

Fig 5. (a) Illustration of the IRV-2 shape. (b) IRV-2 trajectory, dpeicted by altitude and velocity vs flight time. Source: [11].

4.2. Homogeneous and heterogeneous chemistry models

The chemistry model consists of 11 species, namely N_2, O_2, NO, N and O to describe nonionizing air, as well as CO_2, CO, CN, C, C_2, C_3, which come from gas-surface interactions and are fully part of the flowfield. The finite-rate chemistry model used to describe the chemical reactions into the flow (homogeneous chemistry) is based on [20, 21]. The present work takes account of 26 chemical reactions, including dissociation and neutral exchange. The same trajectory has also been computed with the historical ablation model that employs B' tables generated with the same chemical frame.

The finite-rate surface chemistry model (heterogeneous chemistry) considered to compute the mass flow rate includes carbon oxidation and sublimation. In this section, carbon oxidation is described by [22, 23] with the single heterogeneous reaction

$$\mathrm{C(s)} + \mathrm{O_2} \rightarrow \mathrm{CO_2}, \tag{11}$$

which is governed by pseudo-Arrhenius rates

$$\begin{cases} \dot{m}_{\mathrm{O_2}} &= -k_0 \exp\left(-T_a/T\right) \sqrt{P_{\mathrm{O_2}}} \dfrac{M_{\mathrm{O_2}}}{M_{\mathrm{C}}}, \\ \dot{m}_{\mathrm{CO_2}} &= k_0 \exp\left(-T_a/T\right) \sqrt{P_{\mathrm{O_2}}} \dfrac{M_{\mathrm{CO_2}}}{M_{\mathrm{C}}} \end{cases} \tag{12}$$

with $P_i = \rho c_i RT/M_i$ the partial pressure of species i. Carbon sublimation is depicted by [24] via the chemical scheme

$$i\,\mathrm{C(s)} \rightarrow \mathrm{C}_i, \tag{13}$$

with $i = (1, 3)$. More specifically, carbon sublimation is governed by a Knudsen-Langmuir formulation for nonequilibrium surface evaporation. Such reacting law involves both the saturated vapor pressure $\widehat{P}_{\mathrm{C}_i}$ related to the C_i gas species and the partial pressure P_{C_i} of C_i at the wall according to

$$\dot{m}_{\mathrm{C}_i} = \alpha_i \sqrt{\frac{M_{\mathrm{C}_i}}{2\pi RT}} \left(\widehat{P}_{\mathrm{C}_i} - P_{\mathrm{C}_i}\right). \tag{14}$$

In this formulation, the α_i coefficients (for $i = 1, .., 3$) are taken from [25] and $\widehat{P}_{\mathrm{C}_i} = P^0\, 10^{K_{\mathrm{C}_i}^{\mathrm{JANAF}}}$ consistently with the equilibrium wall partial pressure related to the sublimation reaction. The sublimation

rate thus depends on the amount of carbonaceous species already present in the flow and is all the more important as the gas is devoid of C_i. The total mass flow rate $\dot{m}$ is finally given as the contribution of the mass flow rates $\dot{m}_i$ specified for each species produced or consumed at the wall.

To shed some light on the heterogeneous chemistry, Fig. 6 shows the evolution of the species mass fractions vs temperature for a given pressure $P = 10^6$ Pa and a given unblown convective coefficient $\alpha_0 = 10$ kg/m^2/s (left), as well as the evolution of the calculated mass flow rates $\dot{m}$ with temperature, for six different values of α_0 (right). The presented mass fractions and total mass flow rate have been obtained via the resolution of the ODE (8) (chemical equilibrium being considered), with the respective contribution of the blowing $\dot{m}_i$ respectively brought by oxidation (12) and sublimation (14). Here δy is equal to the boundary layer thickness arbitrary set to $\delta y = \delta l_e = 10^{-4}$ m, and with the element mass fraction at boundary layer location imposed to be $\widetilde{c}_e(N) = 0.77$, $\widetilde{c}_e(O) = 0.23$ and $\widetilde{c}_e(C) = 0.00$.

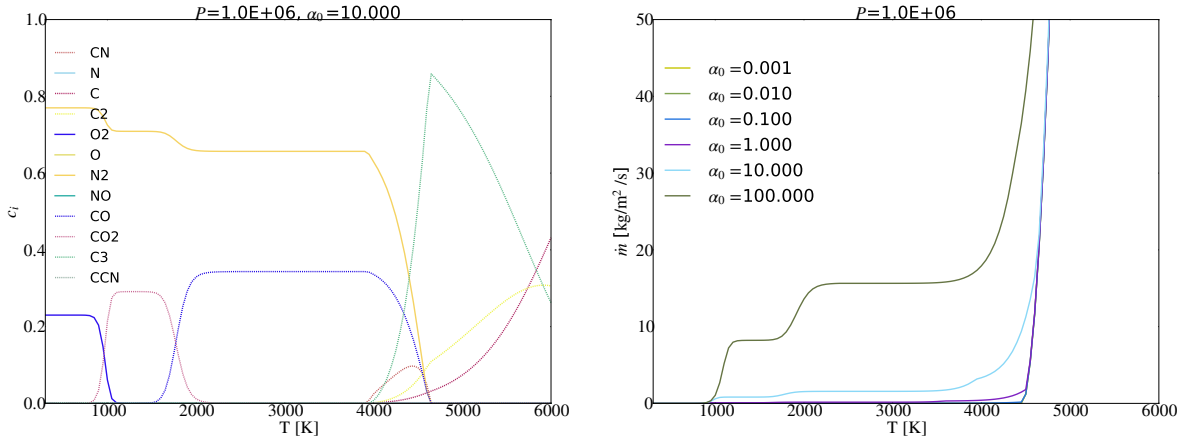

Fig 6. For $P = 10^6$ Pa. (a) Equilibrium species mass fractions vs Temperature. (b) Mass flow rate vs Temperature.

Three regimes of chemical erosion can be distinguishable from Fig. 6.

- For a wall temperature $T_w < 1000$ K, chemical erosion is governed by the kinetics of the oxidation reactions, which are too slow to burn all the oxygen diffusing from the boundary layer to the wall (chemical erosion is said to be kinetic-limited). The mass flow rate thus increases with the wall temperature.
- For $1000 < T_w < 3500$ K, chemical erosion is limited by the oxygen diffusion to the wall (chemical erosion is said to be diffusion-limited). All the oxygen that diffuses to the wall is burnt by carbon. The mass flow rate remains therefore constant as T_w increases. In practice, such regime can be split into two contributions. At low temperatures (1000 K $< T < 2000$ K), oxidation reactions produce CO_2 according to

  $$C(s) + O_2 \rightarrow CO_2,$$

  as highlighted above. For higher temperatures (2000 K $< T < 3500$ K), dissociation of CO_2 occurs in the flow, given rise to CO production. The equivalent heterogeneous reaction can be written as

  $$2C(s) + O_2 \rightarrow 2CO.$$

  Hence, for a given quantity of O_2, twice more carbons are consumed to generate CO than to generate CO_2, which explains the presence of an oxidation plateaus in $\dot{m}$ twice higher for the production of CO than CO_2.
- For $T_w > 3500$ K, carbon sublimation is preponderant, resulting in an ablation rate increasing exponentially with temperature.

4.3. 2D-axisymmetric results

The temperature inside the heat shield of the IRV-2 vehicle at its final trajectory point (time = 21.28 seconds) is shown in Fig. 7, the upper panel representing the computations performed with the historical ablation model (equilibrium gas and tabulated mass flow rates via (7)) and the lower panel being related to the multi-species ablation model. A good agreement is qualitatively observed between both the temperatures as well as the recession surfaces, with a recession nevertheless more pronounced when performed by the historical ablation model. The maximum temperature value inside the solid exceeds 4500 K, which is likely to favor sublimation.

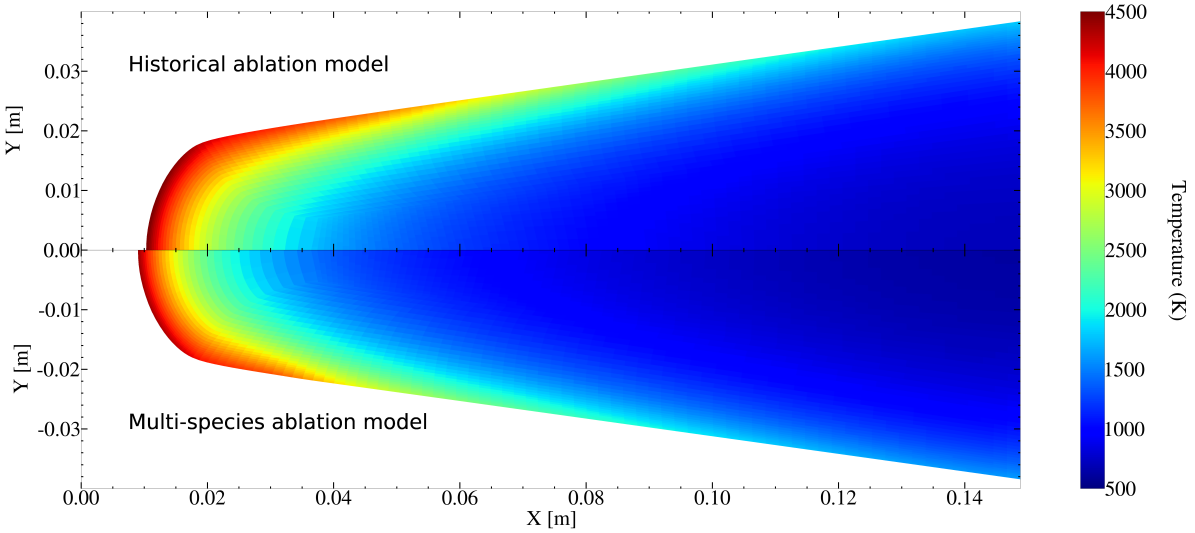

Fig 7. Temperature inside the solid at the final trajectory point for the historical ablation model (upper panel) and the multi-species ablation model (lower panel).

In what follows, comparisons are also made with the results given by the ABRES Shape Change Code (ASCC). The ASCC is an analytical/correlation-based code specifically designed to predicting the performance of ablating nosetips. It incorporates actual flight data in its database and is therefore considered reliable in the framework of ablating axisymmetric sphere-cones [1, 2].

Fig. 8 depicts respectively the evolution of the mass flow rate and surface recession with time at the stagnation point of the IRV-2 vehicle. This is where the heating environment is the most extreme. A good agreement is obtained between the three paradigms (ASCC, historical and multi-species ablation models), either in terms of the time evolution of the ablation rate or surface recession on the stagnation point of the spacecraft.

Significant discrepancies between ASCC data and both ablation models are nevertheless noticeable at the first trajectory points. Fig. 8 emphasizes that the differences produced by the multi-species ablation model with the ASCC data at the beginning and at the end of the trajectory points are somehow compensated, resulting in a final surface recession very similar to the ASCC predictions. More specifically, the multi-species ablation model predicts a mass flow rate of almost zero during the first 10 seconds of the trajectory (corresponding to an altitude from 67 km to 40 km).

To explain such behavior, let us mention that this early flight phase is governed by a kinetic-limited regime for which the diffusion rates are higher than the heterogeneous kinetic rates. Oversimplifying equation (9), this means that the stationary mass fractions at the wall c_i^∞ satisfy $c_i^\infty \approx c_i^1$, where c_i^1 is recalled to be the mass fractions in the vicinity of the vehicle surface (in the first fluid cell). Since the gas is in a strong chemical nonequilibrium at such high altitudes, temperature downstream the shock reaches a peak of 13000 K (not shown). Such high temperature condition triggers the dissociation of molecules to generate N and O, which diffuse from the shock layer to the wall. Such behavior is reported

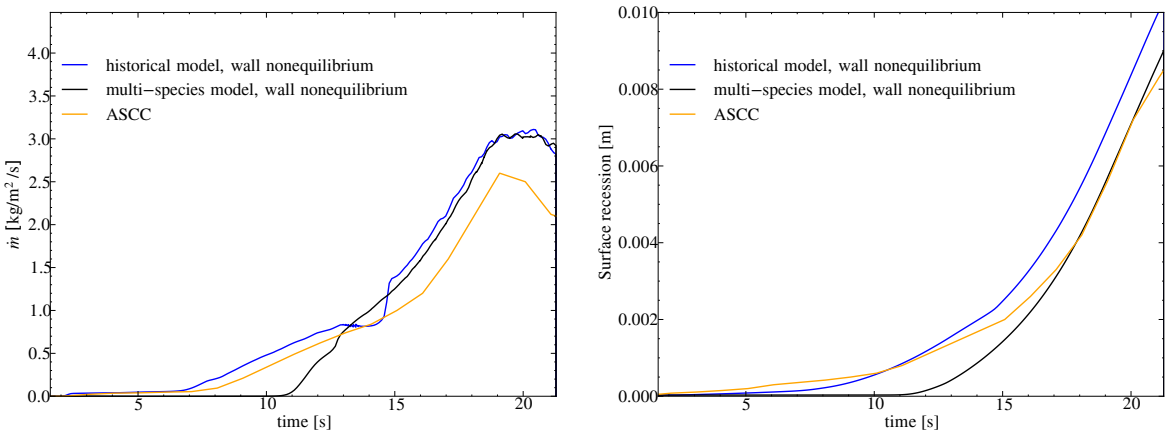

Fig 8. At stagnation point, (a) mass flow rate $\dot{m}$ vs time, (b) surface recession vs time. Results are related to the historical model (blue), the multi-species model (black), and the data taken from ASCC (orange).

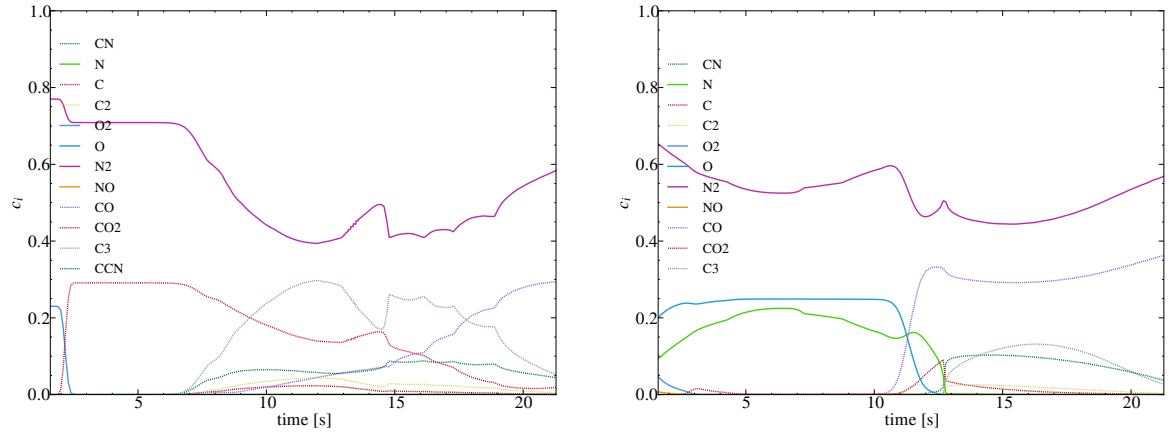

Fig 9. At stagnation point, mass fractions vs time (a) with the historical ablation model, (b) with the multi-species ablation model.

in Fig. 9, which shows the time evolution of the wall species mass fractions at the stagnation point of the IRV-2 vehicle. Inside the boundary layer, even for relatively low temperatures (below 1000 K), the non-negligible presence of N and O is attested, which makes the surrounding air naturally devoid of O_2 ($c^1_{O_2} \approx 0$). Consequently the oxidation reaction (11) at the gas-solid interface between O_2 and graphite carbon cannot be initiated during the first trajectory phase, which explains the very weak values for the mass flow rate in Fig. 8 until a trajectory time of 10 seconds. As for the historical ablation model, the mass flow rate is found to be non-negligible during the same early flight descent. Indeed, for this kinetic-limited regime, Equation (7) tells that the wall mass fraction of O_2 is dominated by the amount of O_2 found at the boundary layer location since $c_i^\infty \approx c_i^e$, the latter being given by the freestream conditions $c^e_{O_2} = 0.23$. Hence the historical ablation model predicts the presence of O_2 at the wall and thus the possibility for the oxidation reactions to occur.

With these physical interpretations in mind, the results from the historical ablation model are found to corroborate better the ASCC results than the multi-species model do at high altitudes. Such observations attest for the need to improve the oxidation model to make the multi species ablation model more predictive, as discussed in the last section.

After a time of 12 seconds (at an altitude of 35 km) the surface temperature increases less significantly and is almost constant after 15 seconds, meaning that an equilibrium is reached between the heat gained by the solid from the gas and the heat removed via ablation. As previously mentioned, the surface temperature does not exceed 4600 K, which is obtained at a trajectory point of 19 seconds (altitude of 10 km).

Considering now the entire trajectory, the historical model nevertheless tends to overestimate the total mass flow rate compared with the multi-species ablation model, resulting in an over-prediction of the final surface recession, as shown in Fig. 8. As mentioned earlier, the mass flow rate overpredicted by the multi-species model is recovered by the underestimation established in the first trajectory phase, producing a total surface recession comparable with the one given by the ASCC.

4.4. Influence of carbonaceous reactions

In order to exacerbate the drawbacks inherent to the historical ablation formulation, the influence of the injection of carbonaceous species that react with the surrounding gas is investigated.

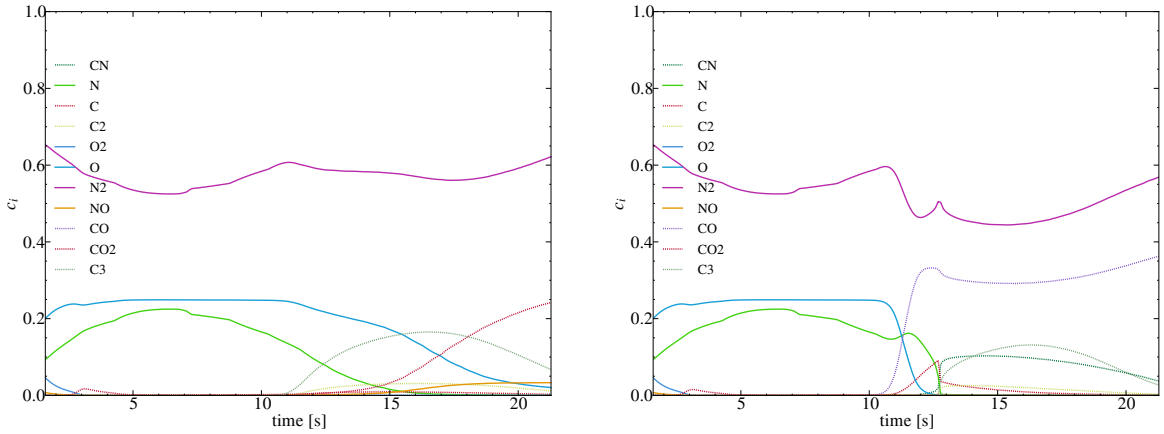

Fig 10. At stagnation point, mass fraction vs time (a) without carbonaceous reactions, (b) with carbonaceous reactions.

Fig. 10 represents the species mass fractions at stagnation point of the IRV-2 vehicle with time when the carbonaceous species are artificially not allowed to react with the surrounding air (left panel) and when the carbonaceous species are completely involved in the reacting scheme (right panel, same as in Fig. 9). As emphasized in Fig. 10, when the carbonaceous reactions are disabled, the only possible carbonaceous species allowed to flow into the gas are the ablation products CO_2 injected via oxidation (11) and C, C_2 and C_3 coming from sublimation (13). Neither CO nor CN species can be produced since their formation comes solely from homogeneous chemistry.

Fig. 11 represents the species mass fractions inside the boundary layer along the stagnation line at the final trajectory point when the carbonaceous species cannot react with the flowfield (left panel) and when the carbonaceous species can chemically interact with the gas (right panel). At first sight, it is clearly seen that the injected carbonaceous species are doomed to diffuse from the wall to the flow when they are treated as non-reacting (dashed lines on left panel), whereas the mass fractions profiles are very different when carbonaceous species take part of the reacting scheme.

The temperature profiles represented for both situations (bottom panel) in Fig. 11 reveals a significant increase of temperature inside the boundary layer when the carbonaceous reactions are allowed compared with the carbon-frozen case. Such feature indicates the occurrence of exothermic carbonaceous reactions in the realistic case. Comparing the mass fractions profiles with the corresponding temperature profiles for both situations, the main exothermic reaction at stakes, which should involve the formation of CO_2

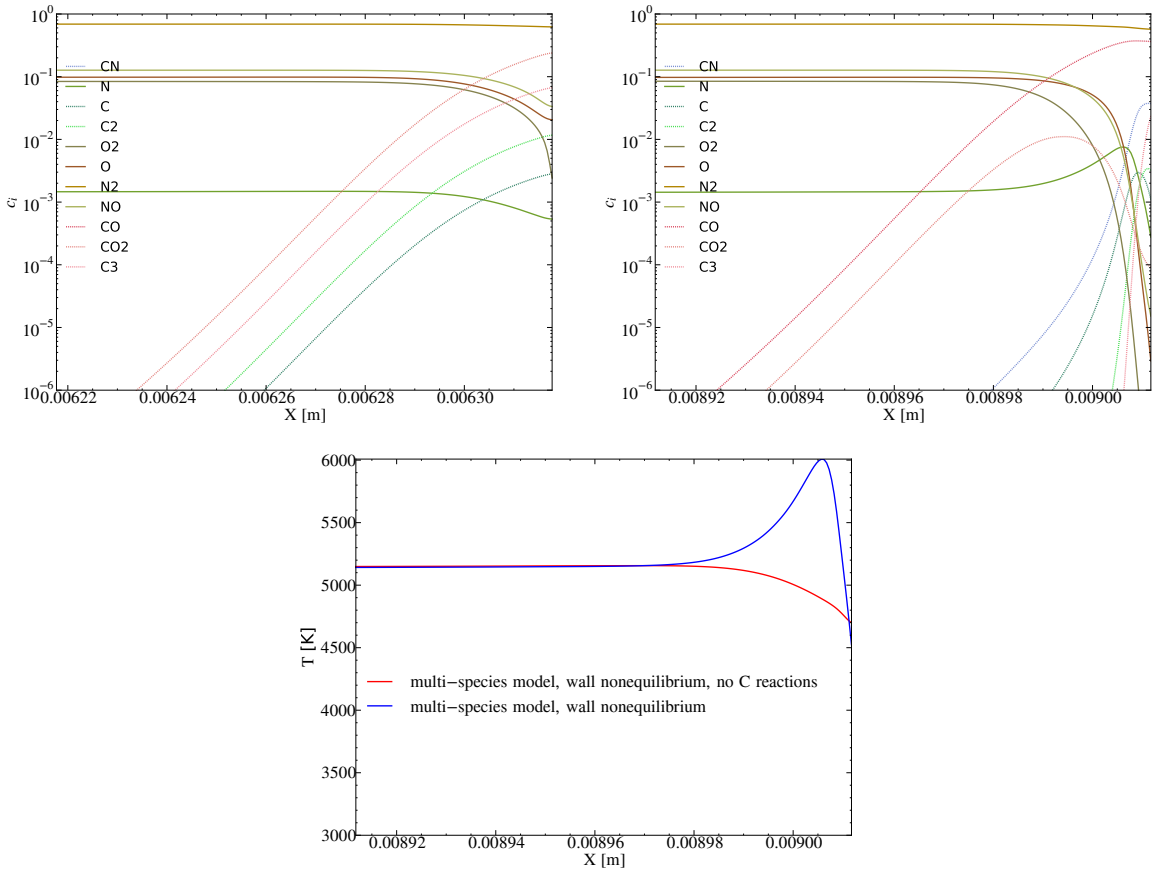

Fig 11. Along stagnation line, (a) mass fractions vs X without carbonaceous reactions, (b) mass fractions vs X with carbonaceous reactions, (c) temperature vs X. The shown temperatures are related to the multi-species ablation model with no carbonaceous reactions allowed within the flow (red) and carbonaceous reactions activated within the flow (blue).

via the recombination of CO, is found to be

$$2\,\mathrm{CO} \rightleftharpoons \mathrm{C} + \mathrm{CO}_2.$$

Such release of heat into the flow via exothermic recombination reactions has a direct impact of the convective wall heat flux, as highlighted by Fig. 12, which shows the temporal evolution of the wall heat flux (upper-left), temperature (upper-right), mass flow rate (bottom-left) and surface recession (bottom-right) at stagnation point of the IRV-2 vehicle.

According to Fig. 12, the calculated convective wall heat fluxes are indeed more important (due to the temperature peak inside the boundary layer) compared with a case for which the carbonaceous chemical reactions have artificially been cut off. The recessing surface is also greater when the carbonaceous species react with the flow: since the injected C_3 species (that are preferentially injected among other carbonaceous species at high temperatures) are mainly consumed by chemical homogeneous reactions, the air is naturally less saturated in C_3, triggering more sublimation according to the Knudsen-Langmuir formulation (14). Such a result attests for the necessity to take account of the injection of carbonaceous species into the flow and their interaction with the ambient gas to accurately predict the wall heat flux and material removal.

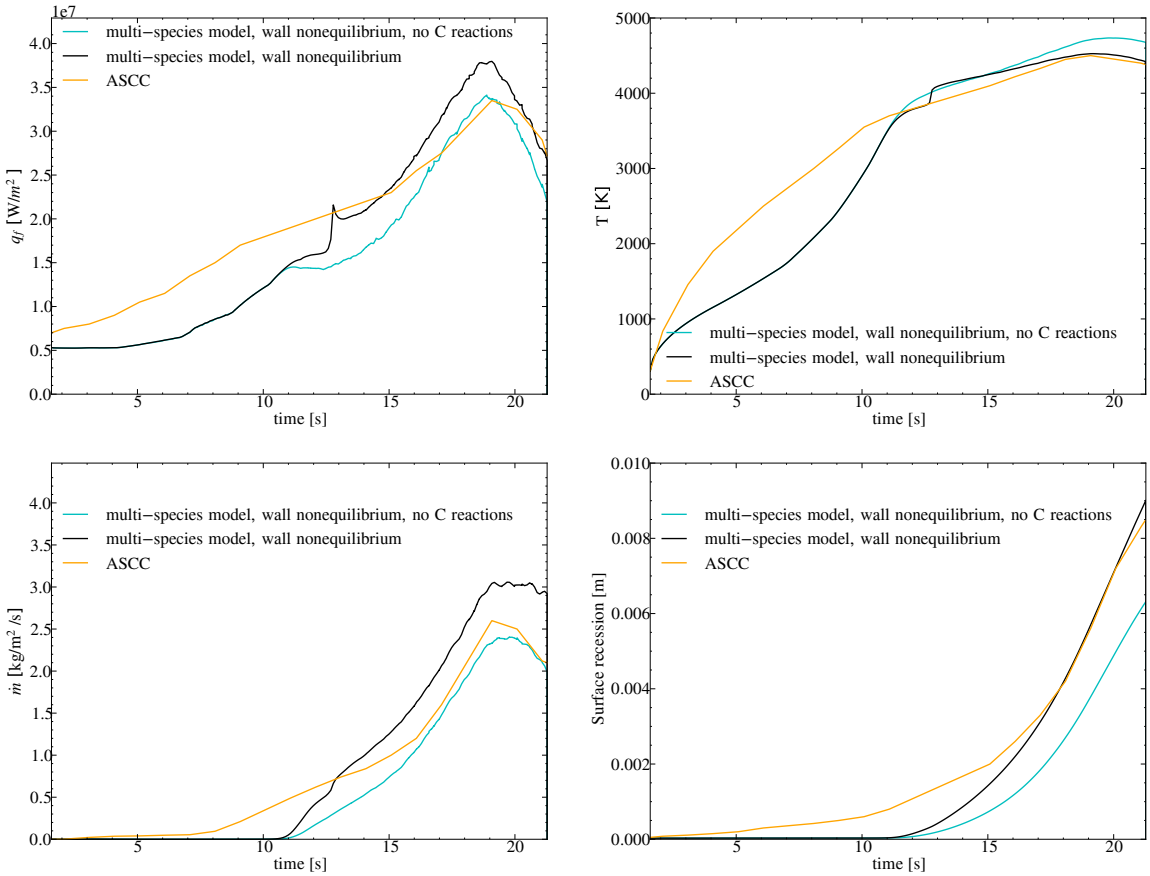

Fig 12. At stagnation point, (a) flux vs time, (b) temperature vs time, (c) mass flow rate vs time, (d) surface recession vs time. Results are related to the multi-species ablation model with no carbonaceous reactions allowed within the flow (cyan), carbonaceous reactions activated within the flow (black), and the data taken from ASCC (orange).

4.5. Equilibrium assumption

Another advantage related to the multi-species ablation model is the generalization to chemical nonequilibrium at the gas-surface interface. Fig. 13 shows the evolution of the mass flow rate (left) and recession surface (right) with time at the stagnation point of the IRV-2 vehicle for two simulations performed with the multi-species strategy imposing either chemical equilibrium at the wall (magenta) and nonequilibrium at the wall (black). ASCC data are also presented.

As illustrated in Fig. 13, simulations for which nonequilibrium prevails leads to reducing the ablated surface thickness compared with the equilibrium situation. Such results indicate that the latter assumption tends to overestimate the ablation rate. Again, the equilibrium hypothesis makes the surrounding flow be devoid of C_3 species (that have been consumed by long-term chemical reactions), which consequently induces higher sublimation rates compared with the more realistic nonequilibrium paradigm. Let us nevertheless mention that the results obtained with chemical equilibrium assumed at the wall are in very good agreement with those given by [8] with the LAURA flow solver for both the mass flow rate and surface recession.

In both cases (equilibrium or nonequilibrium considered at the wall), the gas is treated as a reacting flow (nonequilibrium). As previously put forward, the fluid flowing around the surface is contaminated with mono-atomic species (N and O) that have diffused from hotter regions (typically the shock layer

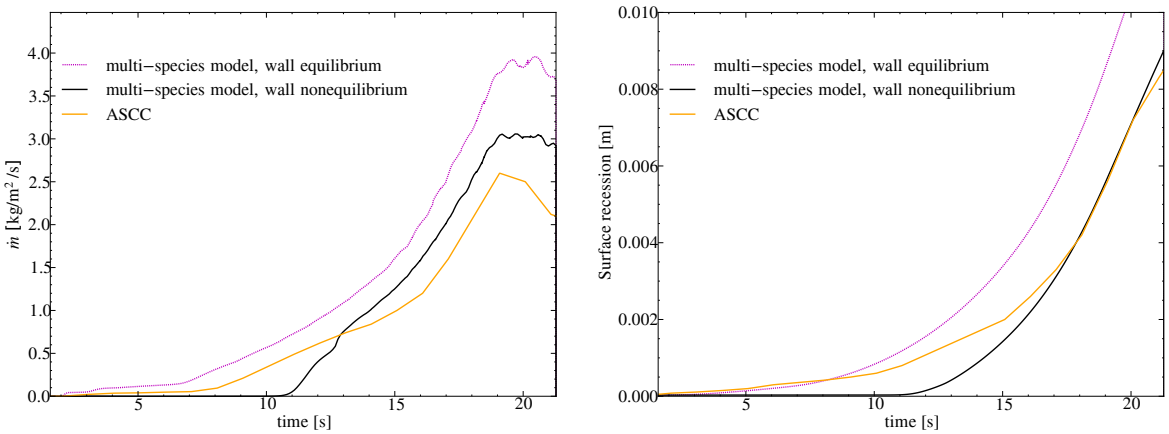

Fig 13. At stagnation point, (a) mass flow rate vs time, (b) surface recession vs time. Results are related to the the multi-species model with equilibrium at the wall (magenta), nonequilibrium at the wall (black) and the data taken from ASCC (orange).

where they have been initially produced via molecule dissociation). Hence, even if the local temperature near the wall is too low to trigger molecule dissociation, the presence of such mono-atomic species at the wall is plausible. In the general situation for which chemical nonequilibrium is considered, the marginal presence of O_2 at the wall disables any possibility for the oxidation reaction (11) to occur. With chemical equilibrium assumed at the wall, however, the mass surface balance equation is solved in terms of element mass fractions instead of species mass fractions, as pointed out by equation (10). Once each element mass fraction at the wall has been calculated, the corresponding species mass fractions are recovered with the use of *Mutation++* with respect to the local wall pressure and temperature [19]. During the trajectory first phase, since the wall temperature is still relatively low, the obtained flow composition is very close to a frozen flow and the equilibrium species at the vehicle surface are thus naturally dominated by N_2 and O_2, as put forward by Fig. 14. More specifically, the presence of O_2 in a significant amount triggers the oxidation reaction (11) and therefore the initiation of graphite material degradation through the ablation process.

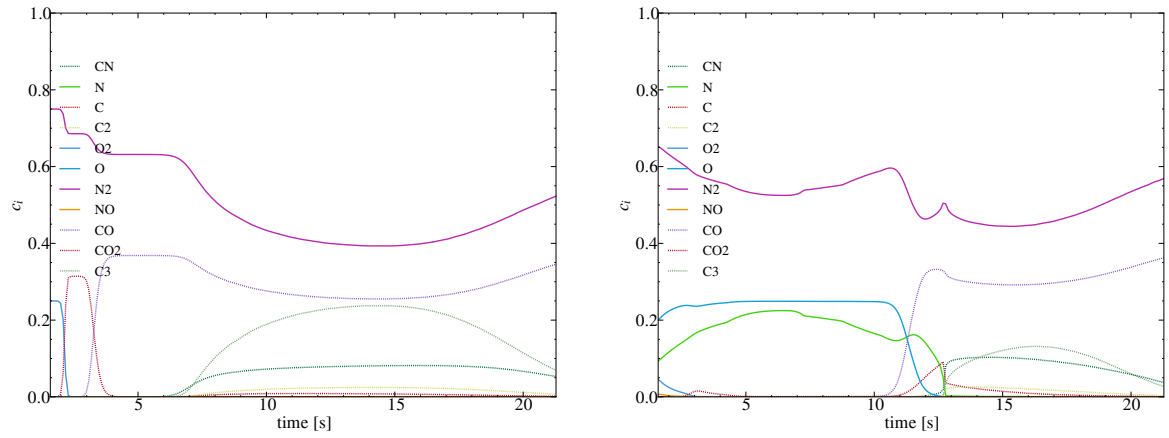

Fig 14. At stagnation point, (a) mass fraction vs time with wall equilibrium, (b) mass fractions vs time with wall nonequilibrium.

4.6. Sensitivity of different oxidation reacting schemes

Since chemical erosion seems to be dominated by oxidation during the first half of the descent trajectory, the sensitivity of different oxidation reactions on the ablated surface shape and temperature is investigated. In this section, a second model used to describe carbon oxidation is considered, which is taken from [26] characterized by the following chemical scheme

$$\begin{cases} \mathrm{C(s)} + \mathrm{O_2} & \rightarrow & \mathrm{CO} + \mathrm{O}, \\ \mathrm{C(s)} + \mathrm{O} & \rightarrow & \mathrm{CO}, \\ \mathrm{C(s)} + 2\mathrm{O} & \rightarrow & \mathrm{C(s)} + \mathrm{O_2}. \end{cases}$$

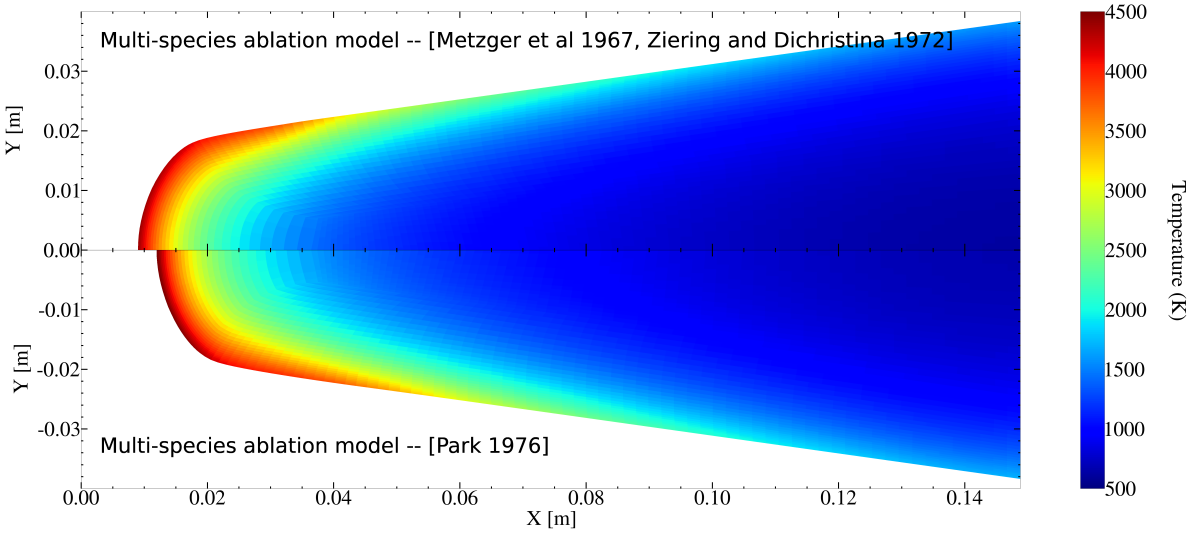

Fig 15. Temperature inside the solid at the final trajectory point for the multi-species ablation model with the oxidation model from [22, 23] (upper panel) and the oxidation model from [26] (lower panel).

The involved carbon mass blowing rates $\widehat{m}_r$ for each oxidation reaction ($r = 1, .., 3$) are expressed by

$$\begin{cases} \widehat{m}_1 &= \rho\, c_{\mathrm{O_2}}\, \beta_{\mathrm{O_2}}\, \bar{\nu}_{\mathrm{O_2}}\, \dfrac{M_{\mathrm{C}}}{M_{\mathrm{O_2}}} \\ \widehat{m}_2 &= \rho\, c_{\mathrm{O}}\, \beta_{\mathrm{O}}\, \bar{\nu}_{\mathrm{O}}\, \dfrac{M_{\mathrm{C}}}{M_{\mathrm{O}}} \\ \widehat{m}_3 &= \rho\, c_{\mathrm{O}}\, \beta_{\mathrm{O}}\, \bar{\nu}_{\mathrm{O}}\, \dfrac{M_{\mathrm{C}}}{2M_{\mathrm{O}}}, \end{cases}$$

with $\bar{\nu}_i = \sqrt{\dfrac{RT}{2\pi M_i}}$ and

$$\begin{cases} \beta_{\mathrm{O_2}} &= \dfrac{1.43 \times 10^{-3} + 0.01\, \exp(-1450/T)}{1 + (2 \times 10^{-4})\, \exp(13000/T)} \\ \beta_{\mathrm{O}} &= 0.63\, \exp(-1160/T). \end{cases}$$

The mass blowing rate $\dot{m}_i$ of each species are then defined by

$$\begin{cases} \dot{m}_{\mathrm{O}} &= \widehat{m}_1 \dfrac{M_{\mathrm{O}}}{M_{\mathrm{C}}} & -\widehat{m}_2 \dfrac{M_{\mathrm{O}}}{M_{\mathrm{C}}} & -2\,\widehat{m}_3 \dfrac{M_{\mathrm{O}}}{M_{\mathrm{C}}} \\ \dot{m}_{\mathrm{O_2}} &= -\widehat{m}_1 \dfrac{M_{\mathrm{O_2}}}{M_{\mathrm{C}}} & +2\,\widehat{m}_3 \dfrac{M_{\mathrm{O_2}}}{M_{\mathrm{C}}} & \\ \dot{m}_{\mathrm{CO}} &= \widehat{m}_1 \dfrac{M_{\mathrm{CO}}}{M_{\mathrm{C}}} & +\widehat{m}_2 \dfrac{M_{\mathrm{CO}}}{M_{\mathrm{C}}}. & \end{cases}$$

Between the two presented oxidation schemes, no pronounced differences on the IRV-2 simulations seem to emerge in terms of vehicle temperature, as put forward in Fig. 15. However, the ablated surface thickness are quite different between both models. Ablation is indeed more pronounced with the use of the oxidation model from [26] than the previously presented one [22, 23].

With the use of this more elaborated oxidation model [26], the physical quantities (mass flux rate and surface recession), which are represented in Fig. 16, are mainly recovered (compared with ASCC) for the first part of the trajectory until 8 seconds (from 67 km to 45 km). This is precisely the phase of flight where the simulations performed with the oxidation model from [22, 23] is deficient. After this first trajectory phase, the model significantly overpredicts the mass flow rate and therefore surface recession compared with the ASCC phenomenological results. Such overestimation is also encountered with the previous model, yet not as striking since it corrects the underestimations of the first flight phase. In terms of surface recession (right panel of Fig. 16), the presented model (oxidation from [26]) matches quite well the results predicted by the historical model. Since the latter, despite its intrinsic limitations, has been fully validated over the past few years, such similarity between both paradigm confirm the physical relevance of the multi-species ablation strategy.

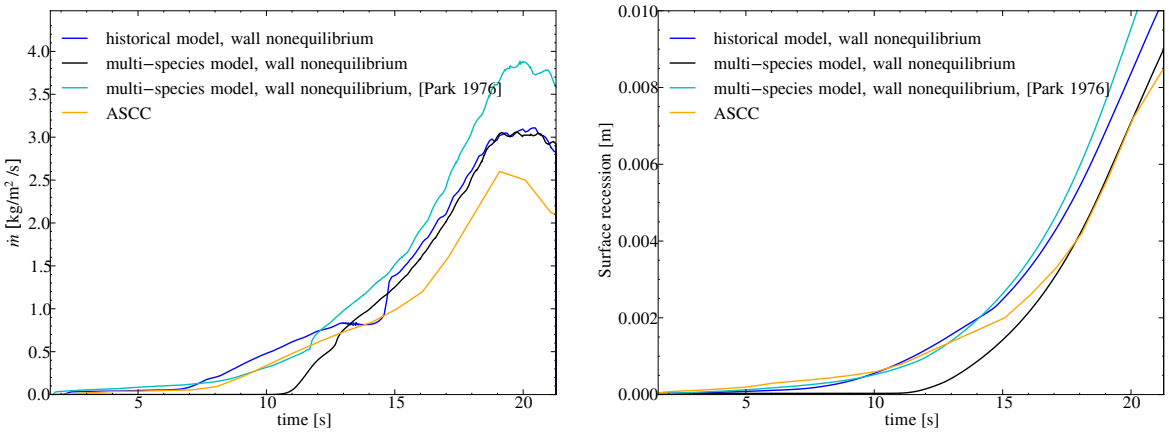

Fig 16. At stagnation point, (a) mass flow rate vs time, (b) surface recession vs time. Results are related to the historical model (blue), the multi-species model with oxidation from [22, 23] (black) and from [26] (cyan), and the data taken from ASCC (orange)

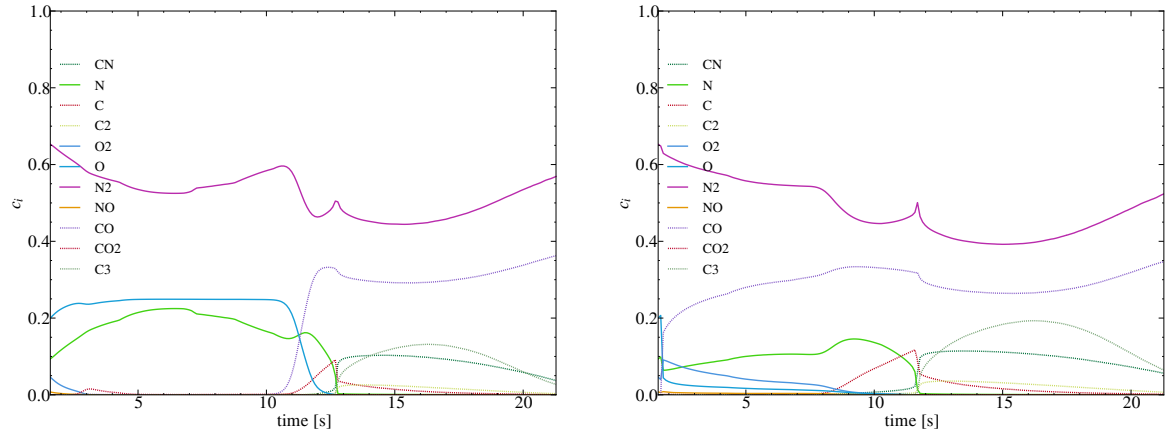

Fig 17. At stagnation point, mass fraction vs time (a) with oxydation model from [22, 23], (b) with oxydation model from [26].

Fig. 17 shows the temporal evolution of the species mass fractions at the stagnation point of the IRV-2 vehicle during its reentry flight, with the oxidation model from [22, 23] (left panel) and with the oxidation model from [26] (right panel). The most obvious difference between the two paradigms is the preponderance of O from $t = 0$ second to $t = 10$ seconds with the first oxidation model, whereas the O species in the second model, for the same trajectory early phase, is almost entirely consumed by oxidation to produce CO. Indeed, the first oxidation model only allows the burning of graphite carbon through its interaction with O_2. The latter species being missing at the wall, no oxidation can occur and thus no ablation as explained earlier. For the second oxidation model however, the graphite carbon can react with O to generate CO and therefore leading to a significant ablation rate from the very beginning of the descent, as emphasized in Fig. 16.

5. Conclusions

In the present work, the derivation of a multi-species ablation model that works in tandem with a Navier-Stokes solver devoted to nonequilibrium reacting flow has been described. The advantages related to such new paradigm are legion. Among them, let us recall the enforcement of the coupling fluid / thermal strategy, making it numerically more robust, as well as the possibility to overcome all the physical limitations related to the commonly used historical mono-species ablation model. In this context, this study has also taken the opportunity to recall and explain the fundamental hypothesis onto which the historical model relies.

The multi-species ablation model presented in this work shows relevant results when applied to the trajectory of the IRV-2 vehicle compared with other reference simulations and flight data. On the whole, the mass flow rates and surface recession are accurately computed in view of the flight data coming from ASCC. More specifically, the lastly presented oxidation model has shown promising results when focused on the first half of the IRV-2 flight trajectory. To this extent, it will be worth to try different sublimation reacting schemes to see if the physics at stakes during the second half of the vehicle trajectory can be captured as well as the oxidation-dominated flight phase. Additionnal kinetics schemes dedicated to homogeneous chemistry can also be tested to include more nitridation products (C_2N, C_2N_2, C_4N_2) within the gas, as well as the consideration of ionized species.

Let us also point out that the close correspondence between the results obtained from the historical (and still reliable) model and the multi-species model has been fully attested in this study, which is a supplementary argument in favor of the consistency of the developed strategy. A drawback of the present method that has not yet been tackled still remains concerning the significant increase of computational time and resources required by the multi-species formulation. Some numerical extensions are currently investigated to alleviate such necessary computing memory (see [27] for example).

In order to conclusively achieve a proper validation of the presented paradigm, the next target is to lead comparisons with experimental data, as made in [28]. Another short-term perspective would be to extend the presented model to other pyrolyzing (charring) ablative materials [29].

References

[1] Hassan, B., Kuntz, D., and Potter, D., "Coupled Fluid/thermal Prediction of Ablating Hypersonic Vehicles," *36th AIAA Aerospace Sciences Meeting and Exhibit*, 1998. https://doi.org/10.2514/6.1998-168.

[2] Kuntz, D. W., Hassan, B., and Potter, D. L., "Predictions of Ablating Hypersonic Vehicles Using an Iterative Coupled Fluid/Thermal Approach," *Journal of Thermophysics and Heat Transfer*, Vol. 15, No. 2, 2001, pp. 129–139. https://doi.org/10.2514/2.6594.

[3] Martin, A., and Boyd, I., "Strongly Coupled Computation of Material Response and Nonequilibrium Flow for Hypersonic Ablation," *41st AIAA Thermophysics Conference*, 2009. https://doi.org/10.2514/6.2009-3597.

[4] Chen, Y.-K., and Milos, F. S., "Two-Dimensional Implicit Thermal Response and Ablation Program for Charring Materials," *Journal of Spacecraft and Rockets*, Vol. 38, No. 4, 2001, pp. 473–481. https://doi.org/10.2514/2.3724.

[5] Chen, Y.-K., and Milos, F. S., "Navier-Stokes Solutions with Finite Rate Ablation for Planetary Mission Earth Reentries," *Journal of Spacecraft and Rockets*, Vol. 42, No. 6, 2005, pp. 961–970. https://doi.org/10.2514/1.12248.

[6] Martin, A., Boyd, I., Cozmuta, I., and Wright, M., "Chemistry Model for Ablating Carbon-Phenolic Material During Atmospheric Re-Entry," *48th AIAA Aerospace Sciences Meeting Including the New Horizons Forum and Aerospace Exposition*, 2010. https://doi.org/10.2514/6.2010-1175.

[7] Martin, A., and Boyd, I. D., "Strongly Coupled Computation of Material Response and Nonequilibrium Flow for Hypersonic Ablation," *Journal of Spacecraft and Rockets*, Vol. 52, No. 1, 2015, pp. 89–104. https://doi.org/10.2514/1.A32847.

[8] Gnoffo, P., and Johnston, C., "A Boundary Condition Relaxation Algorithm for Strongly Coupled, Ablating Flows including Shape Change," *42nd AIAA Thermophysics Conference*, 2012. https://doi.org/10.2514/6.2011-3760.

[9] Johnston, C. O., Gnoffo, P. A., and Mazaheri, A., "Study of Ablation-Flowfield Coupling Relevant to the Orion Heatshield," *Journal of Thermophysics and Heat Transfer*, Vol. 26, No. 2, 2012, pp. 213–221. https://doi.org/10.2514/1.T3769.

[10] Alkandry, H., Boyd, I. D., and Martin, A., "Coupled Flow Field Simulations of Charring Ablators with Nonequilibrium Surface Chemistry," *44th AIAA Thermophysics Conference*, 2013. https://doi.org/10.2514/6.2013-2634.

[11] Farbar, E. D., Alkandry, H., Wiebenga, J., and Boyd, I. D., "Simulation of Ablating Hypersonic Vehicles with Finite-Rate Surface Chemistry," *11th AIAA/ASME Joint Thermophysics and Heat Transfer Conference*, 2014. https://doi.org/10.2514/6.2014-2124.

[12] Chase, M. W., *NIST-JANAF Thermochemical Tables, Fourth Edition*, American Institute of Physics, 1998.

[13] Wilke, C. R., "A Viscosity Equation for Gas Mixtures," *The Journal of Chemical Physics*, Vol. 18, No. 4, 1950, pp. 517–519. https://doi.org/10.1063/1.1747673.

[14] Blottner, F. G., Johnson, M., and Ellis, M., "Chemically Reacting Viscous Flow Program For Multi-Component Gas Mixtures," 1971. https://doi.org/10.2172/4658539.

[15] McBride, B., Zehe, M., and Gordon, S., *NASA Glenn Coefficients for Calculating Thermodynamic Properties of Individual Species*, NASA Technical Paper, National Aeronautics and Space Administration, John H. Glenn Research Center at Lewis Field, 2002.

[16] Martin, A., Zhang, H., and Tagavi, K. A., "An Introduction to the Derivation of Surface Balance Equations Without the Excruciating Pain," *International Journal of Heat and Mass Transfer*, Vol. 115, 2017, pp. 992–999. https://doi.org/https://doi.org/10.1016/j.ijheatmasstransfer.2017.07.078.

[17] Duffa, G., *Ablative Thermal Protection Systems Modeling*, American Institute of Aeronautics and Astronautics, Inc., 2013.

[18] Anderson, J., *Hypersonic and High-temperature Gas Dynamics*, AIAA education series, American Institute of Aeronautics and Astronautics, 2006.

[19] Scoggins, J. B., Leroy, V., Bellas-Chatzigeorgis, G., Dias, B., and Magin, T. E., "Mutation++: MUlticomponent Thermodynamic And Transport properties for IONized gases in C++," *SoftwareX*, Vol. 12, 2020, p. 100575. https://doi.org/https://doi.org/10.1016/j.softx.2020.100575.

[20] Park, C., "Review of chemical-kinetic problems of future NASA missions. I - Earth entries," *Journal*

of Thermophysics and Heat Transfer, Vol. 7, No. 3, 1993, pp. 385–398. https://doi.org/10.2514/3.431.

[21] Park, C., Jaffe, R. L., and Partridge, H., "Chemical-Kinetic Parameters of Hyperbolic Earth Entry," *Journal of Thermophysics and Heat Transfer*, Vol. 15, No. 1, 2001, pp. 76–90. https://doi.org/10.2514/2.6582.

[22] Metzger, J. W., Engel, M. J., and Diaconis, N. S., "Oxidation and Sublimation of Graphite in Simulated Re-entry Environments," *AIAA Journal*, Vol. 5, No. 3, 1967, pp. 451–460. https://doi.org/10.2514/3.4001.

[23] Ziering, M., and Dicristina, V., "Thermomechanical Erosion of Ablative Plastic Composites," *7th Thermophysics Conference*, 1972. https://doi.org/10.2514/6.1972-299.

[24] Lundell, J. H., and Dickey, R. R., "Ablation of ATJ Graphite at High Temperatures," *AIAA Journal*, Vol. 11, No. 2, 1973, pp. 216–222. https://doi.org/10.2514/3.50451.

[25] Zhluktov, S. V., and Abe, T., "Viscous Shock-Layer Simulation of Airflow past Ablating Blunt Body with Carbon Surface," *Journal of Thermophysics and Heat Transfer*, Vol. 13, No. 1, 1999, pp. 50–59. https://doi.org/10.2514/2.6400.

[26] Park, C., "Effects of Atomic Oxygen on Graphite Ablation," *AIAA Journal*, Vol. 14, No. 11, 1976, pp. 1640–1642. https://doi.org/10.2514/3.7267.

[27] Candler, G. V., Subbareddy, P. K., and Nompelis, I., "Decoupled Implicit Method for Aerothermodynamics and Reacting Flows," *AIAA Journal*, Vol. 51, No. 5, 2013, pp. 1245–1254. https://doi.org/10.2514/1.J052070.

[28] Bianchi, D., Nasuti, F., and Martelli, E., "Navier-Stokes Simulations of Hypersonic Flows with Coupled Graphite Ablation," *Journal of Spacecraft and Rockets*, Vol. 47, No. 4, 2010, pp. 554–562. https://doi.org/10.2514/1.47995.

[29] Turchi, A., Bianchi, D., Nasuti, F., and Onofri, M., "A Numerical Approach for the Study of the Gas-surface Interaction in Carbon-phenolic Solid Rocket Nozzles," *Aerospace Science and Technology*, Vol. 27, No. 1, 2013, pp. 25–31. https://doi.org/https://doi.org/10.1016/j.ast.2012.06.003.